Evidence that cerebral blood volume can provide brain activation maps with better spatial resolution than deoxygenated hemoglobin

Joseph P. Culver,[a],* Andrew M. Siegel,[b] Maria Angela Franceschini,[b] Joseph B. Mandeville,[b] and David A. Boas[b]

[a]*Mallinckrodt Institute of Radiology, Washington University School of Medicine, 4525 Scott Avenue, St. Louis, MO 63110, USA*
[b]*Martinos Center for Biomedical Imaging, Massachusetts General Hospital, Harvard Medical School, Charlestown, MA 02129, USA*

With the aim of evaluating the relative performance of hemodynamic contrasts for mapping brain activity, the spatio-temporal response of oxy-, deoxy-, and total-hemoglobin concentrations were imaged with diffuse optical tomography during electrical stimulation of the rat somatosensory cortex. For both 6-s and 30-s stimulus durations, total hemoglobin images provided smaller activation areas than oxy- or deoxy-hemoglobin images. In addition, analysis of regions of interest near the sagittal sinus vein show significantly greater contrast in both oxy- and deoxy-relative to total hemoglobin, suggesting that oximetric contrasts have larger draining vein contributions compared to total hemoglobin contrasts under the given stimulus conditions. These results indicate that total hemoglobin and cerebral blood volume may have advantages as hemodynamic mapping contrasts, particularly for large amplitude, longer duration stimulus paradigms.
© 2005 Elsevier Inc. All rights reserved.

Introduction

The blood oxygenation level dependent (BOLD) signal common to functional Magnetic Resonance Imaging (fMRI) is predominately due to the paramagnetic properties of deoxy-hemoglobin ([HbR]). With high arterial saturation (~99%), appreciable concentrations of [HbR] are generally only present in capillary and venous vessels. One potential problem when mapping neural activity with [HbR] is that significant modulations in [HbR] can occur in larger veins distal and distant to the area of neuronal activation (Frahm et al., 1994). In an effort to over come this problem, MRI methods, such as flow crushing gradients, have been developed to quench the BOLD image contrast in large veins and provide improved mapping of brain

activity (Boxerman et al., 1995). Recent studies using fMRI method alternatives to the BOLD signal indicate that both flow sensitive contrasts (Duong et al., 2002; Kim and Ugurbil, 2003; Lee et al., 2002; Silva et al., 1999) and CBV contrasts (Gautama et al., 2003; Leite et al., 2002; Mandeville et al., 2001; Vanduffel et al., 2001) can provide advantages over the BOLD signal including better contrast to noise ratio, smaller activation areas, and reduced draining vein effect. In this contribution, we use Diffuse Optical Tomography (DOT) to examine the spatio–temporal evolution of [HbR], oxy-hemoglobin ([HbO]), and total hemoglobin ([HbT]) contrasts in response to electrical stimulation of rat forepaw with the aim of determining the relative imaging performance of each contrast.

Results of previous invasive reflectance optical intrinsic signal (OIS) imaging studies suggest a complex dependence of the hemodynamic activation area upon the specifics of the stimulus type. OIS imaging has proven to be an extremely useful technique for imaging brain function, with the advantage of being able to spatially resolve superficial arteries, capillaries, and veins (Grinvald et al., 1986). Early work by Frostig et al. suggested that reflectance OIS measurements at oxygenation sensitive wavelengths ($\lambda = 600-630$ nm) are better localized (smaller activation areas) than reflectance images at a total hemoglobin sensitive wavelength ($\lambda = 570$ nm) during visual stimulus in cats (Frostig et al., 1990). Recent work imaging single whisker stimuli in mice also found smaller activation areas for a deoxy sensitive wavelength ($\lambda = 610$ nm) relative to activation maps at a total hemoglobin wavelength ($\lambda = 540$ nm) (Erinjeri and Woolsey, 2002). On the other hand, Sheth et al. found that the magnitude of CBV related optical measures ($\lambda = 570$ nm) exhibits a stronger correlation with the magnitude of evoked field potential (Sheth et al., 2003) than oximetric ($\lambda = 610$ nm) contrasts, and that both CBV and early time oximetric contrasts were capable of columnar localization in the rat somatosensory cortex (Sheth et al., 2004a). However, OIS results need to be interpreted with caution since they are strongly weighted towards superficial vasculature response. In addition, recent methodological advances, that use more rigorous tissue optic models including a full spectral decomposition with

* Corresponding author. Fax: +1 314 747 5191.
E-mail address: culverj@wustl.edu (J.P. Culver).

appropriate wavelength dependent pathlengths (Devor et al., 2003; Dunn et al., 2003; Kohl et al., 1998; Mayhew et al., 1999; Sheth et al., 2004a), have not yet been used to assess spatial extent. Thus, invasive reflectance OIS characterization of activation areas remains an active area of research.

Non-invasive diffuse optical imaging (DOI) methods, that utilize near infrared spectroscopy have also been used to map both deoxy- and oxy-hemoglobin (Boas et al., 2002; Villringer and Chance, 1997; Yodh and Boas, 2003). As yet, methods equivalent to flow crushing gradients have not been developed for DOI, suggesting that functional imaging of [HbR] with DOI will be adversely affected by contrast in large vessels. However, as with OIS, other DOI hemodynamic contrasts are available. DOI can image both hemoglobin types, and reinterpretation of the two types provides a cerebral blood volume (CBV) measure through the total hemoglobin concentration ([HbT]), and a measure of hemoglobin oxygen saturation (StO_2). DOI methods, including the point measure technique commonly known as Near Infrared Spectroscopy (NIRS), have been used to non-invasively monitor human brain activity during a variety of functional activities, including motor (Franceschini et al., 2003; Obrig et al., 1996; Toronov et al., 2000), visual (Heekeren et al., 1997; Meek et al., 1998; Takahashi et al., 2000), auditory (Chen et al., 2002; Sakatani et al., 1999; Zaramella et al., 2001), and cognitive tasks (Chance et al., 1993; Fallgatter and Strik, 1998; Tsujimoto et al., 2004). In contrast to PET and MRI, DOI does not use a rigid fixed scanner but instead employs a wearable imaging cap. A DOI cap is optimally suited for brain imaging in several novel situations not amenable to scanner geometries, including pediatrics (Chen et al., 2002; Hebden, 2003; Hintz et al., 1999; Kusaka et al., 2001b, 2004; Meek et al., 1998; Sakatani et al., 1999; Taga et al., 2003), and tasks in adults such as studies of gait (Miyai et al., 2001, 2003; Saitou et al., 2000), sleep (Kusaka et al., 2001b; McGown et al., 2003; Spielman et al., 2000), and longitudinal bedside imaging (Hintz et al., 1999; Keller et al., 2000; Kusaka et al., 2001a; Sokol et al., 2000). Typically, DOI methods use a grid of interlaced source and detectors and utilize only nearest neighbor measurements. A more robust tomographic form of imaging, diffuse optical tomography (DOT), employs source-detector pairs with overlapping measurement volumes, such that each detector receives light from multiple distinguishable sources, and data inversion procedures that provide self-consistent solutions among the multiple measurement pairs (Boas et al., 2002; Oleary et al., 1995; Yodh and Boas, 2003). We recently demonstrated that tomographic approaches incorporating both nearest and second nearest neighbor measurements provide significantly improved images compared to the more common interpolation between nearest neighbor only measurements (Boas et al., 2004). In small animal models, where imaging performance is significantly enhanced, volumetric diffuse optical tomography has been used recently to map cerebral hemodynamics during motor function (Culver et al., 2003c; Siegel et al., 2003; Yu et al., 2003), focal ischemia (Bluestone et al., 2004b; Culver et al., 2003b), and global hypoxia and hypercapnia (Bluestone et al., 2004a; Culver et al., 2002).

While insight into the hemodynamic response as measured by DOT can be gained from fMRI and OIS, the point spread functions, depth sensitivities, and vascular compartments weightings to the measured signals, vary significantly between the different brain mapping methods. In addition, DOT of brain activity is relatively new compared to invasive optical imaging and fMRI. The goal of this study was to compare the spatial extents of functional activation maps generated from [HbO], [HbR], and [HbT] contrasts using diffuse optical tomography. To facilitate a comparison with fMRI, we followed the animal preparation and stimulus protocol in a set of previously published fMRI studies in which CBV and BOLD contrasts were used to map the evoked response to stimulation of the rat somatosensory cortex (Mandeville et al., 1998, 1999a, 2001).

Materials and methods

Animal preparations

Adult male Sprague–Dawley rats (300–325 g) were anesthetized (Isoflurane 1–1.5%, N_2O 70%, O_2 30%) and catheters were placed into a femoral artery to monitor the arterial blood pressure and into a femoral vein for drug delivery. The body temperature was maintained at $36.7 \pm 0.5°C$. The animals were tracheotomized, mechanically ventilated, and fixed on a stereotactic frame. The pressure cycled ventilator was adjusted as needed to maintain a nominal end-tidal CO_2 of 38 ± 5 Torr. After surgery, isoflurane was discontinued, and anesthesia was maintained with a 50 mg/kg intravenous bolus of α-chloralose, followed by continuous intravenous infusion of 30–45 mg/kg/h, adjusted to stabilized MAP at 100 ± 10 mm Hg.

Functional activation paradigm

Twenty-seven gauge hypodermic needles cleaned of silicone solvent were attached in pairs across both the right and left forepaws. Stimulation involved 200 µs constant current pulses at 3 Hz repetition, with amplitude 1 or 2 mA. Two pulse trains were used; (a) 6 s stimulation followed by 54 s rest, and (b) 30 s stimulation followed by 90 s rest. Between 8 and 32 blocks were acquired with either the right or the left forepaw individually stimulated.

Diffuse optical tomography instrumentation

These studies employed a frequency-encoded continuous wave imaging system with 9 dual wavelength sources (laser diodes, 9 at 690 nm and 9 at 830 nm) and 16 avalanche photodiode (APD) detectors. The source lasers are square-wave modulated, each at a separate frequency spanning 4–8 kHz, with 200 Hz spacing. Outputs of the 16 APD modules were AC-coupled, amplified and digitally sampled at 16 bits at a rate of 40 ksps. The system provides the following performance: detection sensitivity with a noise equivalent power, NEP $= 0.04 pW/\sqrt{Hz}$ fixed gain dynamic range (linear to 1%) >60 dB, and inter source-detector-pair channel cross-talk <-60 dB. The optode array covered a flat region of the rat head extending 7.5 mm either side of midline, and from 4 mm anterior to 11 mm posterior of bregma. Both the sources and the detectors were coupled through 200 µm fibers to a 25 mm × 25 mm rubber pad (see Fig. 1). The rubber pad was flexible and allowed to conform to the slightly curved geometry of the rat head. The light from each source was detected by all 16 detectors, for a total of 144 source-detector pairs, at both the 690 nm and 830 nm wavelengths. Coupling of the fibers to the tissue was established by monitoring the light levels for each source and detector.
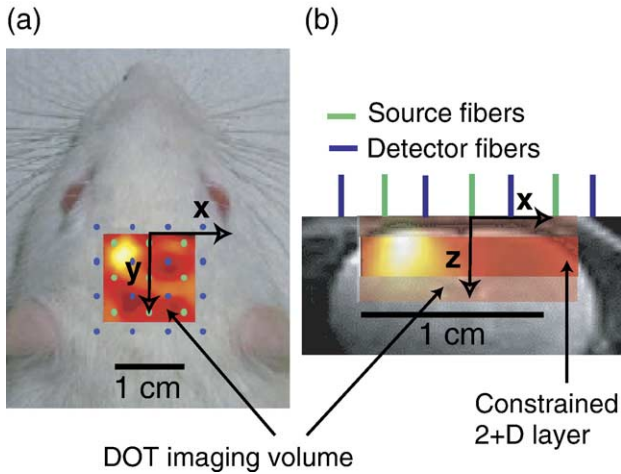
Here, G is the Greens function that models light transport for the given boundary conditions and optical properties. The semi-infinite solution discussed above was used to calculate G. The inverse problem, with Tikhonov regularization, is expressed as minimizing the following objective function:

$$\min\left\{\|\mathbf{y}_{meas} - \mathbf{A}\mathbf{x}\|_2^2 + \alpha\|L\mathbf{x}\|_2^2\right\}. \tag{3}$$

The penalty term for image variance, $\alpha\|L\mathbf{x}\|_2^2$, is a pseudo norm and depth dependent regularization was used where the diagonal of $\mathbf{L} = (\text{diag}(\mathbf{A}^T\mathbf{A}) + \beta)^{1/2}$. A solution, $\mathbf{x} = \mathbf{A}_{\beta,\alpha}^{\#}\mathbf{y}_{meas}$, was obtained using a Moore–Penrose generalized inverse with, $A_{\beta,\alpha}^{\#} = \mathbf{L}^{-1}\tilde{\mathbf{A}}^T(\tilde{\mathbf{A}}^T\tilde{\mathbf{A}} + \alpha\mathbf{I})^{-1}\mathbf{y}_{meas}$, where $\tilde{\mathbf{A}} = \tilde{\mathbf{A}}\mathbf{L}^{-1}$. The values of α and β were optimized to provide even imaging across the field of view as judged by evaluating point, line, and half space objects using a resolution matrix analysis and contrast to noise assessments (Culver et al., 2003a,b). Baseline optical property values were based on previously published data obtained using frequency domain measurements on a group of 5 similarly sized and anesthetized rats (Culver et al., 2003b). The reduced scattering coefficients were, $\mu'_{s,\lambda=690\text{ nm}} = 18\text{ cm}^{-1}$ and $\mu'_{s,\lambda=830\text{ nm}} = 16\text{ cm}^{-1}$. Baseline absorption coefficients ($\mu_{a,\lambda=690\text{ nm}} = 0.21\text{ cm}^{-1}$ and $\mu_{a,\lambda=830\text{ nm}} = 0.22\text{ cm}^{-1}$) were calculated based on values total hemoglobin concentration, [HbT] = 100 μM, and 70% oxygen saturation.

Both three-dimensional and constrained two-dimensional reconstructions of the data were performed. For the three-dimensional reconstructions, an optode positional correction routine was applied prior to reconstruction (Stott et al., 2003). The volumetric domain consisted of cubic voxels 0.5 mm on edge, spanning a $18 \times 18 \times 6$ mm (x,y,z) volume ($\sim 1.5 \times 10^4$ voxels). The light from each source was detected by all 16 detectors, for a total of 144 source detector pairs (SD-pairs), at each of the 690 nm and 830 nm wavelengths. These SD-pairs have separation distances ranging from 3.5 mm to 17.5 mm. For reconstructions, we used the measurements with SD-pair distances <12 mm. This resulted in a set of 100 SD-pairs, 36 of which were nearest neighbors ($\rho_{SD} = 3.5$ mm), 48 at second nearest distance ($\rho_{SD} = 3.5$ mm) and 16 at third nearest distance ($\rho_{SD} = 3.5$ mm). Computation of $\mathbf{A}_{\beta,\alpha}^{\#}$ took 14 s on an 1.8 GHz AMD Athlon™ MP dual processor machine with 2 GB memory. $\mathbf{A}_{\beta,\alpha}^{\#}$ was computed once and then applied to the entire measurement time series. For analysis, we extracted a smaller volume well sampled by multiple SD pairs. The $14 \times 14 \times 4.5$ mm volume extended from 2 mm anterior to 12 mm posterior of bregma, 7 mm laterally of midline on both sides and to a depth of 4.5 mm.

For constrained two-dimensional reconstructions, cubic voxels 0.5 mm on edge, spanning an $18 \times 18 \times 2$ mm volume ($\sim 5 \times 10^3$ voxels) were used with 100 measurements. For analysis, we extracted a $14 \times 14 \times 2$ mm volume extending from +2 mm to −12 mm of bregma, 7 mm either side of midline. Single slice two-dimensional images in the horizontal plane were obtained by averaging the volume along the depth dimension from 1.5 to 3.5 mm. The depth range was chosen based on the results of the volumetric three-dimensional reconstructions (see Results; Culver et al., 2003c) and through comparison with fMRI results (Mandeville and Marota, 1999; Mandeville et al., 2001).

Time series concentration images

Prior to image inversion, the source detector data were low pass filtered to 2 Hz. The baseline intensity data for each channel (I_0

Fig. 1. Diffuse optical tomography (DOT) imaging schematic. The light to and from the rat head is relayed by 16 detector fibers and 9 bi-wavelength source fibers. The array covers a 15 mm by 15 mm square area on the flat portion of the rat head. The imaging domains are shown in both (a) horizontal (xy) and (b) coronal (xz) views. A volumetric imaging domain was used to confirm the depth of activation. The 3D image constrained to and integrated over depths of 1.5 to 3.5 mm was used for the subsequent spatio-temporal analysis.

Reconstructing hemoglobin concentrations

We modeled diffuse photon density waves using an extrapolated zero boundary, semi-infinite media solution (Haskell et al., 1994). The diffuse wave fluence rate, Φ_i, for the ith source and detector pair measurement with source position, $\mathbf{r}_{s,i}$, and detector position, $\mathbf{r}_{d,i}$, is,

$$\Phi(\mathbf{r}_{s,i},\mathbf{r}_{d,i}) = \frac{3\mu'_s S_0}{4\pi}\left(\frac{e^{-kr_1}}{r_1} - \frac{e^{-kr_2}}{r_2}\right). \tag{1}$$

The attenuation coefficient, k, is defined, $k^2 = 3\mu'_s(\mu_a - i\omega/v)$, where, μ_a is the tissue absorption coefficient, μ'_s is the tissue scattering coefficient, ω is the source modulation frequency, v is the speed of light in the medium, and S_0 is the point-source amplitude and phase. The distances to the real source, $r_1 = |\mathbf{r}_{s,i} - z\hat{\mathbf{z}} - \mathbf{r}_{d,i}|$, and the image source, $r_2 = |\mathbf{r}_{s,i} + (z + 2z_B)\hat{\mathbf{z}} - \mathbf{r}_{d,i}|$, are defined by a source depth, $z_0 = 1/\mu'_s$, and $z_B = 2/3\mu'_s$ the extrapolated zero boundary distance.

Differential image reconstructions were obtained using a linear Rytov approximation approach (Kak and Slaney, 1988). In this scheme, the total diffuse wave fluence, Φ, is written as, $\Phi = \Phi_0 \exp(\Phi_{scat})$. The total fluence, Φ, consists of a background field, Φ_0, that depends on background optical properties, and a perturbed field, Φ_{scat}, which is linearly related to a set of spatial variations in the optical properties $\delta\mu_a$ and $\delta\mu'_s$. Experimental measurements of Φ on the sample surface lead to images of the spatially varying absorption via solution of a least-squares problem. In this work, we utilize the intensity data to reconstruct absorption perturbations. The Rytov formulation of the scattered field is written in discrete notation as $\mathbf{y} = \mathbf{A}\mathbf{x}$ with the following definitions (Culver et al., 2001; Oleary et al., 1995):

$$y_i = \ln\left[\frac{\Phi(\mathbf{r}_{s,i},\mathbf{r}_{d,i})}{\Phi_0(\mathbf{r}_{s,i},\mathbf{r}_{d,i})}\right],$$

$$A_{i,j} = -\frac{vh^3}{D_0}\frac{G(\mathbf{r}_{s,i},\mathbf{r}_j)G(\mathbf{r}_j,\mathbf{r}_{d,i})}{G(\mathbf{r}_{s,i},\mathbf{r}_{d,i})} \text{ and } x_j = \partial\mu_{a,j}. \tag{2}$$

$(\mathbf{r}_{s,i}, \mathbf{r}_{d,i})$) were defined as the mean value of the data for 2 s preceding T_0. Time series differential data, computed for each channel using, $y_i(t) = \ln|I(\mathbf{r}_{s,i}, \mathbf{r}_{d,i}, t) / I_0(\mathbf{r}_{s,i}, \mathbf{r}_{d,i}, t)|$, were then reconstructed for differential absorption ($\Delta\mu_{a,\lambda\,=\,690\,nm}(r_j, t)$, and $\Delta\mu_{a,\lambda\,=\,830\,nm}(r_j, t)$). The absorption coefficients were converted into hemoglobin concentrations (C) using spectral decomposition; $\Delta\mathbf{C} = \mathbf{E}^{-1}\Delta\boldsymbol{\mu_a}$, where $\Delta C = \{\Delta[HbR], \Delta[HbO]\}$ is a vector of concentrations, $\mathbf{E}$ is a matrix containing the extinction coefficients of [HbR] and [HbO$_2$] at the two wavelengths, and $\Delta\boldsymbol{\mu_a}$ is a vector (i.e. $\Delta\boldsymbol{\mu_a} = \{\Delta\mu_a^{690\,nm}, \Delta\mu_a^{830\,nm}\}$) containing the differential absorption coefficients. The individual hemoglobin concentrations were subsequently converted into a total hemoglobin concentration $\Delta[HbT] = \Delta[HbR] + \Delta[HbO]$. We used published spectra for [HbR] and [HbO] for the extinction coefficients (Prahl, 2002; Wray et al., 1988). Image time series were subsequently averaged using temporal bins, with $\delta T_{bin} = 2$ s, for both the $T_{stim} = 6$ s and $T_{stim} = 30$ s data.

Data analysis

The temporal standard deviation of each pixel was calculated from 10 s of 2 Hz baseline data. Dividing the time series concentration images by the corresponding standard deviation images, we obtained time series images of contrast to noise ratio (CNR). Here, noise is defined as the standard deviation in the baseline images. The CNR image time series were subsequently averaged using temporal bins, with $\delta T_{bin} = 2$ s, for both the $T_{stim} = 6$ s data, and $T_{stim} = 30$ s data. The CNR magnitudes of the averaged data were adjusted from the 2 Hz standard

deviation values by assuming that the standard deviation scaled with SD $\sim 1/\sqrt{(N)}$, where N = number of 2 HZ samples in the averaged temporal bin. Specifically, SD ($\delta T_{bin} = 2$ s) = SD (2 Hz) / 2.

To gain insight into the spatio-temporal evolution of each hemodynamic contrast, we processed the time series images in two ways. First, time traces were extracted for four regions of interest (ROIs), spaced laterally relative to midline. The ROIs were arranged around peak activation contrast with rectangular volumes of dimension 3.5 mm × 1 mm × 2 mm.

The spatial extent of the activation was quantified by identifying and summing activated pixels greater than 50% maximum contrast. For a two-dimensional Gaussian activation, the number of pixels >50% maximum equals the area defined by the full-width half maximum (FWHM). The time traces of the number of activated pixels >50% of peak value were generated for each data set.

Results

Three-dimensional reconstructions offer the advantage of not requiring an assumption of activation depth. As reported previously, the measurement set obtained is capable of supporting volumetric three-dimensional reconstructions (Culver et al., 2003c). The disadvantage of volumetric reconstructions is that the increased solution space also increases the influence of noise. To produce volumetric images, we used large 6 s temporal bins. Fig. 2 depicts a representative three-dimensional CNR
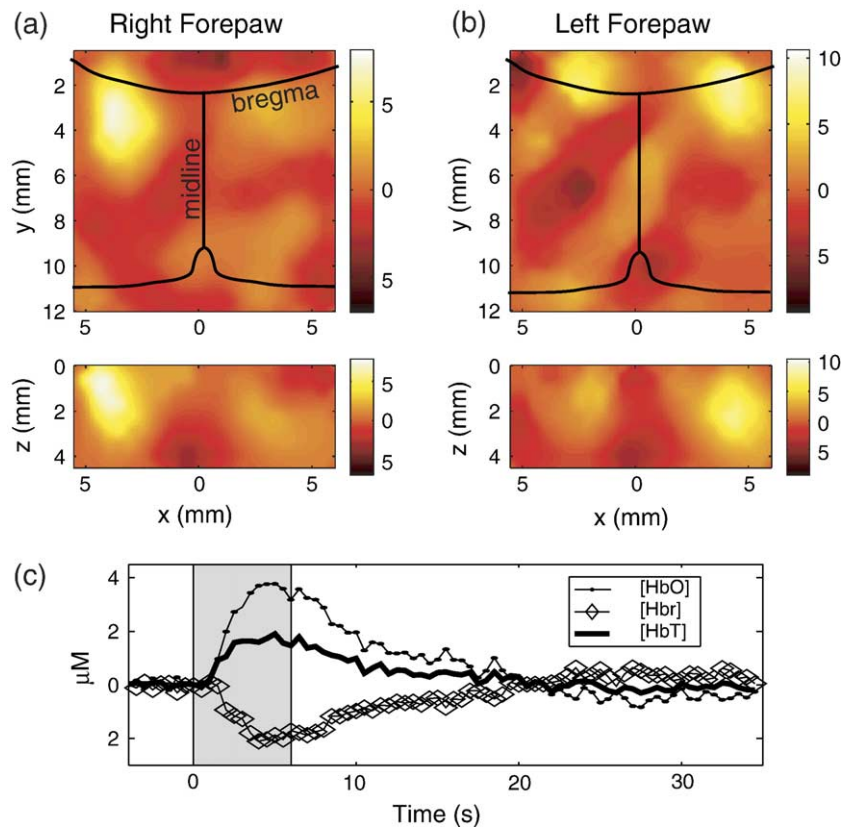

Fig. 2. Experimental volumetric images of rat brain activity. (a) Right forepaw stimulation. Image intensity represents CNR. (b) Left forepaw stimulation. Image intensity represents CNR. (c) Time traces of the hemodynamic response ([HbR], [HbO], [HbT]) for the activation volume.

image of the differential absorption at $\lambda = 830$ nm during electrical stimulation (1 mA for 6 s) of the right (Fig. 2a) and left (Fig. 2b) forepaw. Time courses of the hemoglobin concentrations in the activation volume (2 mm × 2 mm × 2 mm) centered on the peak value were extracted and plotted in Fig 2c. These volumetric images average data from $t = 3$ to 9 s. They demonstrate the contra-lateral activation expected, and the locations of the activations are similar to previously published fMRI images by several groups (Hyder et al., 1994; Mandeville and Marota, 1999; Silva et al., 1999). The details regarding these volumetric images have been discussed previously (Culver et al., 2003c). For further analysis of the comparison of hemodynamic contrasts and their spatio-temporal evolution, we used reconstructions constrained to the cortical layer. The constrained reconstructions were less sensitive to measurement noise and facilitated a two-dimensional spatio-temporal analysis at higher temporal and spatial resolutions than provided by the unconstrained reconstructions. In the layer constrained reconstructions, or 2D images (Fig. 3), ipsi-lateral activations were not evident. In contrast, the 3D images of Fig. 3 show apparent ipsi-lateral activation though at very low CNR (CNR ~3–5). The reason for the differences between the 2D and 3D images is most likely due to the increased image noise in the 3D images that results from the smaller regularization constant needed to resolve the activation in the z dimension. However, fMRI studies in our laboratory have also observed small stimulus-correlated signal changes in ipsi-lateral somatosensory cortex (unpublished), so the 3D results presented here may properly reflect the neurobiology. Future studies with higher signal to noise ratios and denser optode arrays may shed light on these potential ipsilateral activations.

6-s stimulus

Time series concentration images for a representative 6-s stimulus are depicted in Fig. 3 for a single rat. The characteristic increase in oxy hemoglobin, decrease in deoxy-hemoglobin, and increase in total hemoglobin are observed. At $t = 5$ s, all three contrasts (Δ[HbT], Δ[HbR], and Δ[HbO]) clearly show a focal response (Fig. 3) located near the forepaw area of the somatosensory cortex (~4 mm lateral of midline) (Mandeville and Marota, 1999).

While concentration images provide a physiologic variable, statistical images have several advantages. In an addition to providing a quantitative assessment of signal quality, for diffuse optical tomography, the statistical weighting can also improve the image fidelity (Culver et al., 2003c). Contrast to noise ratio (CNR) images corresponding to the concentration images are also presented in Fig. 3, rows d–f. Significant activation (peak activation CNR > 4) contrast is present in the 3, 5, 7 and 9 s frames. The Δ[HbR] activation shifts towards midline relative to Δ[HbO], and both Δ[HbO] and Δ[HbR] appear to shift towards midline as they progress. In contrast, Δ[HbT] activation remains relatively stationary throughout the time series.

To further examine the spatio-temporal evolution of the hemodynamic response, we extracted the hemodynamic response for five ROIs (Fig 4). The ROIs (1 × 3.5 × 2 mm) were arranged in 1.5 mm steps laterally from midline and indexed consistent with the ROIs a–d going from (a) furthest from midline to (e) nearest to midline. The time courses of the hemoglobin concentrations for each ROI were extracted from 5 rats with stimulus of the right forepaw with 2 mA stimulus amplitude for a combined total of 5 data sets (see Table 1). The five data sets were then averaged to
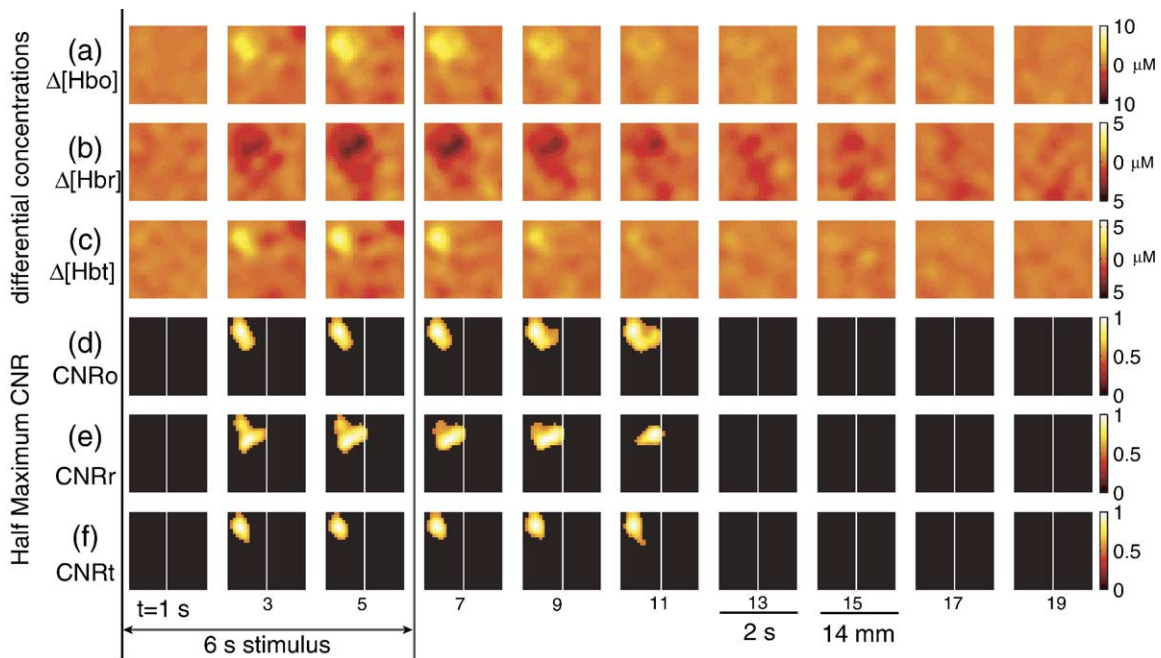

Fig. 3. Time series images of the hemodynamic response to 6 s right forepaw stimulation. Each frame represents a horizontal slice at a depth of 2.5 mm as depicted in Fig. 1. Images represent a binned 2 s average centered at the indicated time for each of the three differential hemoglobin responses (a) Δ[HbO], (b) Δ[HbR], and (c) Δ[HbT]. The concentration (μM) images are plotted using color scales held fixed throughout the time course and indicated at the end of each row. The bottom three rows depict a contrast to noise analysis (d) CNR_O, (e) CNR_R, and (f) CNR_T. The CNR images are individually scaled relative to maximum intensity and a threshold of 50% maximum is applied.
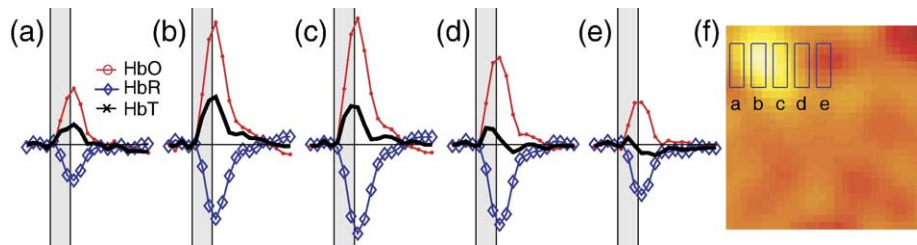
Fig. 4. Hemodynamic time courses versus position for 6 s stimulus. Five regions of interest (ROIs) (labeled a–e) were defined at varying distances from midline (f). Time traces for each ROI were averaged across 5 rats (see text). The time traces nearest the activation (b–c) show the expected trends in Δ[HbO], Δ[HbR], and Δ[HbT]. The time trace nearest midline shows a much reduced Δ[HbT] signal, while the individual Δ[HbO] and Δ[HbR] traces remain elevated.

generate time traces of Δ[HbO], Δ[HbR] and Δ[HbT] (Figs. 4a–e). In the ROI closest to midline (Fig. 4e), activation contrast in both Δ[HbO] and Δ[HbR] remains after $t > 6$ s, while the Δ[HbT] time course in ROI-e shows less activation relative to ROIs b and c. This observation can be quantified by considering the ratios of the contrasts in the ROIs, divided by the contrast in ROI-b, the ROI corresponding to the peak of the [HbT] signal (Fig. 5a). The time courses of each of the ROIs in Fig. 4 were integrated over the times 2–14 s and then divided by the integrated contrast in ROI-b to generate the normalized contrasts plotted in Fig 5a. For Figs. 5a–c, error bars represent standard error in the mean of the distribution in values from the 5 data sets. Significantly smaller normalized contrasts are present in [HbT] compared to [HbR] ('*' for $P < 0.05$, paired t test), and [HbO] ('○' for $P < 0.05$, paired t test) for ROIs c–e. Clearly, the [HbR] and [HbO] contrasts are shifted towards midline relative to [HbT] (ROIs c–e).

The CNR image series were also analyzed for magnitude and activation area as a function of time. The CNR magnitude time course (Fig. 5b) peaks at approximately the same time ($T = 5–6$ s) as the hemodynamic concentration magnitudes and all three hemodynamic variables have similar CNR magnitude. To compare the relative spatial extent of the hemodynamic variables, the activation area was calculated as a function of time (Fig. 5c). Significantly ($P < 0.05$, paired t test) smaller activation areas are present in the CNR_T compared to CNR_R for times 6–14 s, and in CNR_T compared to CNR_O for times 4–8 s. Note that the [HbT] activation area is smaller during the times while CNR is maximum. Details of the activation area for each of the individual five data sets are provided in Table 1. Activation

areas represent an average of the time period from 4 to 14 s post stimulus.

30-s stimulus

A representative image series for the 30-s stimulus protocol is shown in Fig. 6 for a single rat. From the full 2-s sampling time course, we extracted every third frame so as to illustrate the dominant temporal features of each stimulus paradigm and keep the total number of frames in Figs. 3 and 6 equivalent. At $t = 9$ s, all three contrasts ([HbO], [HbR], and [HbT]) clearly show a focal response (Fig. 6) located near the forepaw area of the somatosensory cortex (4–6 mm lateral of midline). At $t > 15$ s, a single focal [HbT] increase remains at the $t = 9$ s location. However, [HbR] and [HbO₂] images begin to show increased contrast towards midline and a central feature develops along midline coincident with the sagittal sinus vein. Notably, both the concentration and CNR [HbT] images remain better localized with a much less pronounced central feature.

An ROI analysis for the same ROIs used with the 6 s data is shown in Fig. 7. Data for the ROIs were averaged over 4 rats for the 30-s stimuli (Table 1). The time courses of ROI-e show an enhanced slow feature. After the stimulus, there is a pronounced undershoot of [HbO] and overshoot of [HbR], while [HbT] returns more slowly to baseline. These post-stimulus transients are evident in concentration images, Figs. 6a–c, but not in the CNR images Figs. 6d–f. The thresholding of the CNR images was applied only to positive contrasts for CNR_O and CNR_T, and to negative contrast for CNR_R, and so the CNR_O undershoot and CNR_R undershoot do not appear in the Figs. 6d–f image series. As with the 6 s data,

Table 1
Results from individual rats for both stimulus durations

| 6 s stimulus (dt = 2–14)						30 s stimulus (dt = 4–30)					
Rat	Forepaw	mA	Area (mm^2)			Rat	Forepaw	mA	Area (mm^2)		
			HbO	HbR	HbT				HbO	HbR	HbT
a	R	2	14.4	18.7	10.4	a	R	2	24.0	17.5	14.8
b	R	2	11.4	18.8	11.1	c	R	2	13.7	20.9	10.4
c	R	2	14.9	14.8	10.3	d	R	2	19.4	20.1	12.8
d	R	2	17.9	17.3	10.5	e	R	2	19.6	26.7	11.1
e	R	2	19.6	20.5	11.7						
Mean value			15.6	18.0	10.8				19.2	21.3	12.3
Standard deviation			3.2	2.1	0.6				4.2	3.9	2.0
Standard error			0.8	0.5	0.2				1.4	1.3	0.7
P value relative to HbT			0.0340	0.0007					0.0143	0.045	
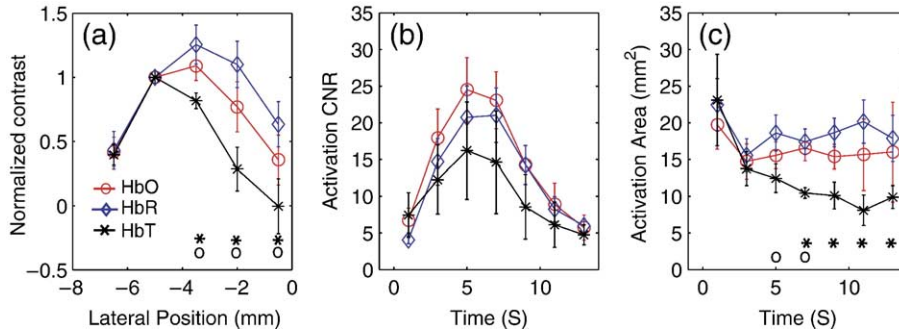
Fig. 5. Comparison of the spatial extent of the hemodynamic responses of [HbO], [HbR] and [HbT]. (a) Normalized contrasts averaged over times 2–14 s as a function of distance from the midline for ROIs a–e in Fig. 4. Contrasts are normalized to the value of ROI-b. Elevated [HbO] and [HbR] concentrations are evident in the regions near midline, towards the sagittal sinus vein. (b) Magnitude of the peak contrast to noise ratio magnitudes (CNR$_O$, CNR$_R$, CNR$_T$) as a function of time. (c) The spatial extent of CNR$_O$, CNR$_R$, and CNR$_T$ activations as a function of time, calculated as the area with CNR above 50% maximum value. Error bars represent standard error in the mean (SEM). Statistical significance of paired t tests ($P < 0.05$) is indicated by 'O' for comparisons between HbT and HbO and by '*' for comparisons between HbT and HbR.

enhanced and delayed contrast for [HbO] and [HbR] in ROI-e nearest midline is concurrent with a significantly smaller relative [HbT] contrast. This observation can be quantified with the same approach used for the 6-s stimulus data (Fig. 5a). The time courses of each of the ROIs in Fig. 7 were integrated over the times 2–30 s and then divided by the integrated contrast in ROI-b to generate the normalized contrasts (Fig 8a). For Figs. 8a–c, error bars represent standard error in the mean of the distribution in values from the 4 data sets. Significantly smaller normalized contrasts are present in [HbT] compared to [HbR] ('*' for $P < 0.05$, paired t test), and

[HbO] ('O' for $P < 0.05$, paired t test) for ROIs c–e. Similarly to the 6-s stimulus results, the [HbR] and [HbO] contrasts are shifted towards midline relative to [HbT] (ROIs c–e).

The CNR magnitude and activation area time courses are shown in Figs. 8b–c. All three hemodynamic variables have similar CNR magnitudes. Details of the activation area for each of the individual four data sets are provided in Table 1. Activation areas in Table 1 represent an average of the time period from 4 to 30 s from beginning of the stimulus. The time averaged activation area of [HbT] is significantly smaller ($P < 0.05$) than both the
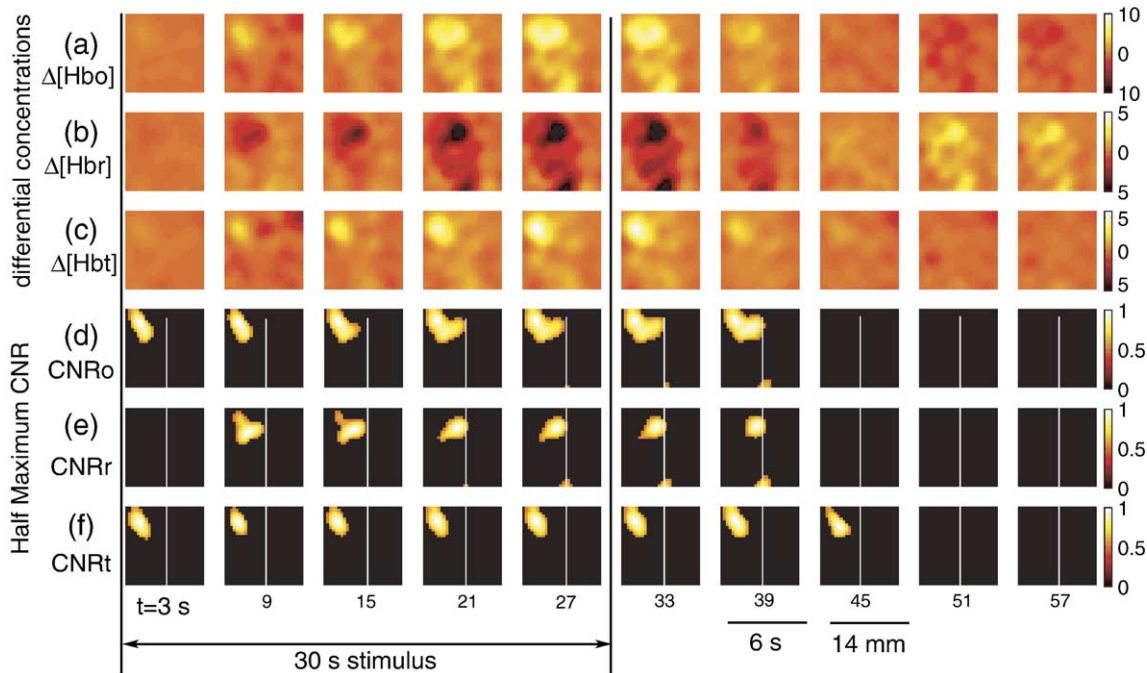

Fig. 6. Representative time series images of the hemodynamic response to 30 s right forepaw stimulation. Each frame represents a horizontal slice at a depth of 2.5 mm as depicted in Fig. 1. Images represent a binned 2 s average centered at the indicated time for each of the three differential hemoglobin responses (a) Δ[HbO], (b) Δ[HbR], and (c) Δ[HbT]. The concentration images are plotted using color scales that are held fixed throughout the time course and indicated at the end of each row. The bottom three rows depict a contrast to noise analysis (d) CNR$_O$, (e) CNR$_R$, and (f) CNR$_T$. The CNR images are individually scaled relative to maximum intensity and a threshold of 50% maximum is applied.
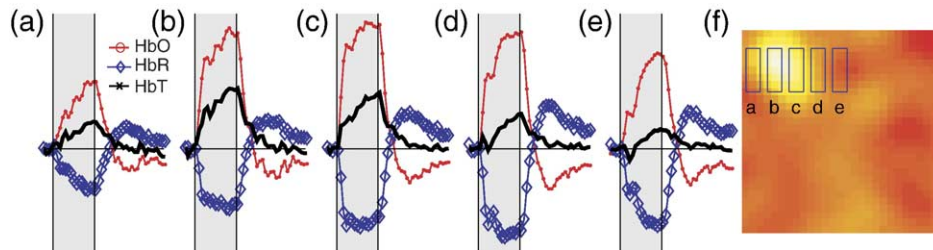
Fig. 7. Hemodynamic time courses versus position for 30 s stimulus. Five regions of interest (ROIs) (labeled a–e) were defined at varying distances from midline (f). Time traces for each ROI were averaged across 4 rats (see text). The time traces nearest the activation (b–c) show the expected trends in Δ[HbO], Δ[HbR], and Δ[HbT]. The time trace nearest midline shows a much reduced Δ[HbT] signal, while the individual Δ[HbO] and Δ[HbR] traces remain elevated.

[HbR] and [HbO] activation areas. Statistical significance ($P <$ 0.05, paired t test) was also observed for several individual time bins between 4 and 30 s (Fig. 8c).

Discussion

Summary of main findings

Time traces for [HbT], [HbR], and [HbO$_2$], all show robust activation in the forepaw area (Figs. 2–8) and are in qualitative agreement with fMRI studies of CBV and BOLD during similar stimulation paradigms (Mandeville et al., 1999a). In previous studies, we examined the temporal correlation of [HbR], [HbO], and [HbT] with fMRI measures of BOLD and CBV during similar rat stimulus paradigms (Siegel et al., 2003). We found strong temporal correlations between both [HbT] and CBV, and BOLD and [HbR]. In the present study, we are interested in the spatial extent of the individual contrasts and find significant differences between the spatio-temporal responses of [HbR], [HbO], and [HbT]. Our main findings are that [HbT] activation areas are smaller than [HbR] and [HbO] activation areas, and that the contrasts of [HbR] and [HbO] are more elevated (or shifted) towards midline relative to [HbT]. In particular, elevated contrast in [HbR] and [HbO] is present in the regions near the sagittal sinus vein through which the cortical blood drains. Although we did not have an electrophysiological correlate for our data, these observations suggest two aspects about the hemodynamic responses under the presented stimulus conditions. First, if we

assume that the hemodynamic response is larger than (or equal to) the underlying neuronal activity, then the hemodynamic contrast with the smallest activation (HbT) can be considered to provide better spatial resolution for functionally mapping neural activity. Secondly, the pial arteries that feed the cortex come up from the sides of the brain, and the venous network drains blood towards the sagittal sinus at midline. Based on this known vascular anatomy, and the known location of forelimb somatosensory cortex, our result showing a shift in contrast of [HbR] and [HbO] towards midline relative to [HbT] suggests that the oxygen sensitive contrasts have enhanced venous draining components relative to [HbT]. In the following discussion, we compare our results to previous measurements of activation areas, discuss the possible mechanistic explanations for the observed differences, and discuss the relation of activation areas to other performance measures including the correlation between the hemodynamic measures and electrophysiology.

Comparisons to invasive optical imaging

Early work by Frostig et al. showed that both predominately oxygenation sensitive ($\sim$600 nm), and CBV sensitive (570 nm) optical reflectance images provide fine detail ($\sim$100 μM) maps of the cortical architecture in the cat visual cortex (Frostig et al., 1990). Subtracting activation images of one eye from the other, they found that a $\sim$600 nm reflectance signal was "more localized to the site of spiking neurons than the blood volume change." It was proposed that this mapping performance results from early oxygen consumption that subsequently initiates a flow response.
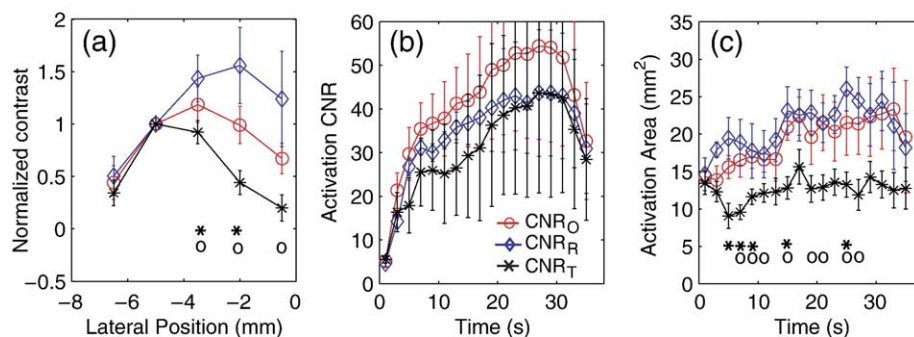

Fig. 8. Comparison of the spatial extent of the hemodynamic responses of [HbO], [HbR], and [HbT]. (a) Normalized contrasts averaged over times 4–30 s as a function of distance from the midline for ROIs a–e in Fig 7. Contrasts are normalized to the value of ROI-b. Elevated [HbO] and [HbR] concentrations are evident in the regions near midline, towards the sagittal sinus vein. (b) Magnitude of the peak contrast to noise ratio magnitudes (CNR$_O$, CNR$_R$, CNR$_T$) as a function of time. (c) The spatial extent of CNR$_O$, CNR$_R$, and CNR$_T$ activations as a function of time, calculated as the area with CNR above 50% maximum value. Error bars represent standard error in the mean (SEM). Statistical significance of paired t tests ($P < 0.05$) is indicated by 'O' for comparisons between HbT and HbO and by '*' for comparisons between HbT and HbR.

More recent in vivo optical microscopy by Erinjeri et al. examined the hemodynamic response during single and two whisker stimuli in the mouse and found the activation extent at early times to be smaller for a deoxy sensitive wavelength ($\lambda = 610$ nm) relative to activation maps at a total hemoglobin wavelength ($\lambda = 540$ nm) (Erinjeri and Woolsey, 2002). It was noted that the measured spatial extent was in large part determined by blurring due to the significant size of superficial arterioles and venules relative to the underlying barrel neural structures. These results do not necessarily translate to larger activation volumes (like rat forepaw) in which the activated tissue volume is larger than feeding arterioles and draining venules.

In contrast, our results show smaller activation areas with [HbT]. There are several methodological differences between the OIS studies and our DOT study that may explain the apparent discrepancy. In our measurements, we observe statistically equivalent activation areas for [HbR], [HbO], and [HbT] for the first time point in the 6-s stimulus protocol (Fig. 5b), averaged over 0–2 s. During the later phase of the response, where CNR peaks, we find a smaller activation area in [HbT] relative to the oxygenation sensitive [HbR] and [HbO] contrasts. Most reports of smaller activations with oximetric contrasts examined activations during the early portion of the hemodynamic response (with lower CNR). As the hemodynamic response develops, the draining vein affects can become more pronounced, and [HbT] can provide a smaller activation area (Figs. 4 and 7). A recent OIS comparison by Sheth et al. also concludes that the timing at which the map is generated can strongly effect the relative mapping performance of the different hemodynamic contrasts (Sheth et al., 2004a).

Different spatial sampling profiles may also influence the comparative results of OIS and DOT. Most previous invasive microscopy is highly biased towards the tissue surface with penetration depths ranging from 100–300 μm for wavelengths from 500 nm–700 nm (Kohl et al., 2000). However, the electrically active cortical layer IV is at a depth of ~400 μM in a rat. Thus, OIS measurements are biased towards feeding arterioles and draining venules above the primary activation site. In contrast, the current DOT measurements use separated source-detector pairs, near infrared wavelengths, and photon migration models to significantly extend depth sensitivity to greater than 3 mm. While performed non-invasively through intact scalp and skull, the DOT images are more evenly weighted throughout the first 2 mm of the cortical tissue than OIS measurements. Recently, Vanzetta et al. have evaluated the use of principal component analysis image processing methods in conjunction with OIS measurements to remove the high resolution superficial vascular components of CBV sensitive images (Vanzetta et al., 2004). These efforts to mitigate the superficial bias of reflectance OIS increased the subsurface sensitivity and resolution of differential CBV maps and permitted the generation of single-condition CBV maps of awake primates under visual stimulus. OIS measurements without such image processing may exaggerate the spatial extent of CBV activation.

In addition to differences in methodology between the current DOT measurements and OIS imaging, there are also significant differences between the physiological protocols. Several OIS studies used smaller and shorter duration stimuli, such as single whisker flicks. As pointed out by Erinjeri et al., the scale of the activation unit relative to the scale of the supporting vasculature can affect the resulting spatial extent of each hemodynamic variable differently (Erinjeri and Woolsey, 2002). For highly localized brain activations such as a single mouse whisker barrel,

the blurring due to the vasculature may be more pronounce for CBV rather than oximetric measures. For larger activations such as a rat forepaw or stimuli in humans, where the activated neural volume is larger compared to the feeding arteriole size, the hemodynamic blurring maybe more pronounced in the oxygen sensitive draining vein effects rather than the [HbT] contrast.

Comparison to previous fMRI and diffuse optical hemodynamic activation area studies

The draining vein contrast is well documented for BOLD signals (Boxerman et al., 1995; Frahm et al., 1994). Commonly used fMRI protocols, with block designs or general linear models, use the entire hemodynamic response. Considerable efforts and advances have been made towards reducing large vessel signals in the BOLD signal, e.g. using flow crushing gradients (Boxerman et al., 1995). More recently, fMRI methods of measuring CBF and CBV have been compared to BOLD contrasts. For example, Mandeville et al. (Mandeville and Marota, 1999) examined CBV weighted and BOLD activations during forepaw stimulus. Analysis of the distribution along a vertical direction (our z direction) found a significant dorsal shift 0.44–0.66 mm in the BOLD activation relative to the CBV activation and statistically equivalent second moments (FWHM). While the cross-sections in the lateral direction were not analyzed, the images presented indicate the BOLD activation may be larger than the CBV activation in the lateral projection. In addition, there appears to be a slight shift in the BOLD signal towards midline similar to the shifts we see (Figs. 3–8). Silva et al. (1999) combined continuous arterial spin labeling with a single-shot, multislice echo-planar imaging to simultaneous image BOLD and CBF changes during electrical rat forepaw stimulation. They found BOLD activation maps significantly larger than CBF maps. Similarly, Duong et al. (2001) imaged the cerebral blood flow response using flow sensitive alternating inversion recovery techniques and found that both CBF measures and early negative bold signals provide increased spatial resolution compared to the late BOLD signal. Our results indicate that HbT can provide improved spatial resolution compared to oximetric contrasts such as BOLD, [HbR], and [HbO], particularly during the delayed peak CNR of a relatively large amplitude hemodynamic response.

Franceschini et al. (2003) have used diffuse optical imaging with back projection image reconstruction algorithms to image the somatosensory response during electrical stimulation of the median nerve in humans. Activation areas were found to be statistically equivalent between CBV, [HbR], and [HbO]. We note that the DOT method used on the rat data in this paper produces higher fidelity images than typical backprojection techniques. In addition, due to the smaller geometry of the rat head, we were able to use an extended range of source-detector separations compared to the single source detector separation imaging employed in the human studies. These added imaging advantages provide for better resolution of the concentration changes.

Possible mechanisms for differences in activations maps for [HbT], [HbR], and [HbO]

Recent efforts to characterize neurovascular coupling depict a complex biochemical signaling process in which neurons, interneurons, and astrocytes induce vasodilatation generating a hyperemic cerebral blood flow response (Iadecola, 2004; Peng et al.,

2004; Zonta et al., 2003). The differential hemoglobin responses are subsequently driven by the increased CBF supplying oxygen rich blood and a proportionally smaller increase in the cerebral metabolic rate of oxygen (CMRO2). While predicting the spatio-temporal evolution of the differential concentrations is challenging, several recent studies have demonstrated the success of balloon (Buxton and Frank, 1997; Buxton et al., 1998; Obata et al., 2004) and windkessel models (Mandeville et al., 1999b). In fMRI experiments, using a vascular contrast agent, the time response for CPV (cerebral plasma volume) has been shown to be significantly different from BOLD signal (Leite et al., 2002). The temporal differences were also shown in rats, and analyses in monkeys routinely rely upon a different impulse response function for CPV than BOLD signal (Mandeville et al., 1999a, 2001). Leite et al. decomposed the CPV kinetics and found that 80% of the CPV signal evolved more slowly than BOLD signal. This provides evidence that CPV signals are dominated by contributions from the slower venous and capillary beds rather than the faster arterial dilation. Our data also show slower dynamics for [HbT] compared to [HbO] and [HbR] (Fig. 7). However, for shorter stimuli, the faster components can be emphasized relative to the slower components. Comparing our short (6 s) and long (30 s) stimuli data, one might expect to see differences associated with the different contributions of slow and fast response elements. However, our data do not show a shift in [HbT] towards midline or increased activation size as one might expect from an enhanced slower venous contribution for the longer stimuli.

Several other experimental studies indicate that the differential [HbT] response to increase CBF can be weighted towards the arterial supply side, while the differential saturation difference is preferentially weighted towards the venous draining side (Erinjeri and Woolsey, 2002; Lee et al., 2001). While resting state CBV is weighted towards the venous side, the dynamic changes can be larger on the arteriole side. Erinjeri et al. have also shown that the vascular architecture mapped with the CBV changes correlated with the arterial supply and that the oxygenation changes correlated with the structure of the draining venules. Thus, the mechanism of arterial weighted ΔCBV and venule weighted differential saturation for brief stimuli, is consistent with both the mouse whisker data and our larger amplitude rat forepaw 6-s stimuli response results.

The observed temporal undershoot of [HbO], overshoot of [HbR], and slow return to baseline of [HbT] also provide insight in to the possible mechanisms affecting the hemodynamic response. We have commented on these features previously and briefly review here (Siegel et al., 2003). Based upon an observed temporal mismatch between CBV and flow, it has been postulated that blood volume is elevated only in the venous compartment during the post-stimulus overshoot of [HbR] following stimulation (Mandeville et al., 1999b). However, if the capillary compartment is also elevated post-stimulus, this could consistently explain the [HbT], [HbO], and [HbR] time courses. In a diffusion-limited model of oxygen delivery from the blood to brain tissue (Buxton and Frank, 1997), elevated capillary blood volume provides a mechanism to increase oxygen delivery even if CBF has returned to baseline. Thus, [HbT] would show a slow post-stimulus decay due to a slow response of both capillary and venous CBV, and the mechanism of the [HbR] overshoot and [HbO] undershoot would be attributed to both elevated CBV and an increased rate of oxygen utilization (CMRO2).

In addition to spatial extent, several studies have evaluated how well the magnitude of the different hemodynamic contrasts correlates to the magnitude of electrical measures of neural activity

including spiking activity and local field potentials. Devor et al. found approximately power law relations between the electrical measures, multiple unit activity (MUA), and summed local field potentials (ΣLFP) and the hemodynamic measures, [HbO] and [HbT] (Devor et al., 2003). Sheth et al. analyzed the correlation of both the early and late oximetric and [HbT] sensitive images with electrophysiology while stimulus amplitude and frequency were varied. Their results suggest that [HbT] correlates well with the summed evoked potentials (ΣEP) whereas oximetric contrasts were not consistently correlated (Sheth et al., 2003). Possibly, the differences observed between the hemodynamic measures are, in part, due to differences in signal to noise ratio. The details of the wavelengths chosen or the measurement noise performance of the optical instrument will strongly influence the correlation coefficients retrieved. A subsequent paper analyzed parametric relations between hemodynamic contrasts and electrophysiology concluding that [HbT] showed a more linear coupling than oximetric contrasts (Sheth et al., 2004b). Nemoto et al. (2004) showed with a trial-by-trial correlation analysis that the CBV related optical signals were more highly correlated with summer field potentials on a per trial basis, than were oxygenation-derived signals. Together, the OIS studies suggest that [HbT], relative to oximetric contrasts, is as well or better correlated with electrophysiological measures of neural activity.

Conclusion

Our experimental results suggest that, for stimulation durations of ~6 s or greater, [HbT] provides a more focal and stationary activation area compared with [HbR], and [HbO] particularly as measured with diffuse optical techniques. These results apply to stimuli of duration ~6 s and relatively strong amplitude (ΔCBV = 4%, volume ~2 mm) and occur during time points near the peak in temporal contrast. Earlier OIS findings that [HbR] is better localized may be due to analyzing activation maps during the very early, lower CNR response window, using stimulus protocols with smaller activation areas relative to the surrounding vascula-ture, or due to the superficial weighting of the OIS reflectance method which can enhance larger feeding and draining vessel signals. Our finding of smaller [HbT] activation area is also consistent with and supports the notion that ΔCBV is more tightly coupled than oximetric measures to the arterial vasodilation that drives the hemodynamic response to neural activation. Combined with the results of Sheth et al. and Nemoto et al., showing superior correlation between [HbT] electrophysiology, and Leite et al., showing improved fMRI contrast to noise ratio for CPV versus BOLD, these results suggests that, for several imaging modalities, [HbT] has several advantages as a functional brain mapping contrast over the oximetric contrasts. Collectively, these results have direct implications for functional imaging with diffuse optical techniques. As well as informing strategies for optimizing func-tional maps, they also suggest that recent efforts to synthesize the cerebral metabolic rate of oxygen consumption (CMRO$_2$) from optical measures may need to account for the differences in spatial extent of each hemodynamic contrast (Ances et al., 2001; Boas et al., 2003; Culver et al., 2003b; Durduran et al., 2004a,b; Mayhew et al., 1999). In addition, they suggest that diffuse optical tomography may be useful for understanding BOLD signals, particularly in human studies that could benefit from the additional [HbT] information provided by DOT.

Acknowledgments

References

Ances, B.M., Wilson, D.F., Greenberg, J.H., Detre, J.A., 2001. Dynamic changes in cerebral blood flow, O-2 tension, and calculated cerebral metabolic rate of O-2 during functional activation using oxygen phosphorescence quenching. J. Cereb. Blood Flow Metab. 21, 511–516.

Bluestone, A.Y., Stewart, M., Lasker, J., Abdoulaev, G.S., Hielscher, A.H., 2004a. Three-dimensional optical tomographic brain imaging in small animals: Part 1. Hypercapnia. J. Biomed. Opt. 9, 1046–1062.

Bluestone, A.Y., Stewart, M., Lei, B., Kass, I.S., Lasker, J., Abdoulaev, G.S., Hielscher, A.H., 2004b. Three-dimensional optical tomographic brain imaging in small animals: Part 2. Unilateral carotid occlusion. J. Biomed. Opt. 9, 1063–1073.

Boas, D.A., Franceschini, M.A., Dunn, A.K., Strangman, G., 2002. Noninvasive imaging of cerebral activation with diffuse optical tomography. In: Frostig, R.D. (Ed.), In Vivo Optical Imaging of Brain Function. CRC Press, Boca Raton, pp. 193–221.

Boas, D.A., Strangman, G., Culver, J.P., Hoge, R.D., Jasdzewski, G., Poldrack, R.A., Rosen, B.R., Mandeville, J.B., 2003. Can the cerebral metabolic rate of oxygen be estimated with near-infrared spectroscopy? Phys. Med. Biol. 48, 2405–2418.

Boas, D.A., Chen, K., Grebert, D., Franceschini, M.A., 2004. Improving the diffuse optical imaging spatial resolution of the cerebral hemodynamic response to brain activation in humans. Opt. Lett. 29, 1506–1508.

Boxerman, J.L., Bandettini, P.A., Kwong, K.K., Baker, J.R., Davis, T.L., Rosen, B.R., Weisskoff, R.M., 1995. The intravascular contribution to fMRI signal change: Monte Carlo modeling and diffusion-weighted studies in vivo. Magn. Reson. Med. 34, 4–10.

Buxton, R.B., Frank, L.R., 1997. A model for the coupling between cerebral blood flow and oxygen metabolism during neural stimulation. J. Cereb. Blood Flow Metab. 17, 64–72.

Buxton, R.B., Wong, E.C., Frank, L.R., 1998. Dynamics of blood flow and oxygenation changes during brain activation: the balloon model. Magn. Reson. Med. 39, 855–864.

Chance, B., Zhuang, Z., Unah, C., Alter, C., Lipton, L., 1993. Cognition-activated low-frequency modulation of light-absorption in human brain. Proc. Natl. Acad. Sci. U. S. A. 90, 3770–3774.

Chen, S., Sakatani, K., Lichty, W., Ning, P., Zhao, S., Zuo, H., 2002. Auditory-evoked cerebral oxygenation changes in hypoxic-ischemic encephalopathy of newborn infants monitored by near infrared spectroscopy. Early Hum. Dev. 67, 113–121.

Culver, J.P., Ntziachristos, V., Holboke, M.J., Yodh, A.G., 2001. Optimization of optode arrangements for diffuse optical tomography: a singular-value analysis. Opt. Lett. 26, 701–703.

Culver, J.P., Durduran, T., Cheung, C., Yodh, A.G., Takahashi, K., Greenberg, J.H., 2002. Diffuse optical measurement of hemoglobin and cerebral blood flow in rat brain during hypercapnia, hypoxia, and cardiac arrest. Adv. Exp. Med. Biol. 510, 48.

Culver, J.P., Choe, R., Holboke, M.J., Zubkov, L., Durduran, T., Slemp, A., Ntziachristos, V., Chance, B., Yodh, A.G., 2003a. Three-dimensional diffuse optical tomography in the parallel plane transmission geometry: evaluation of a hybrid frequency domain/continuous wave clinical system for breast imaging. Med. Phys. 30, 235–247.

Culver, J.P., Durduran, T., Furuya, D., Cheung, C., Greenberg, J.H., Yodh, A.G., 2003b. Diffuse optical tomography of cerebral blood flow, oxygenation and metabolism in rat during focal ischemia. J. Cereb. Blood Flow Metab. 23, 911–923.

Culver, J.P., Siegel, A.M., Stott, J.J., Boas, D.A., 2003c. Volumetric diffuse optical tomography of brain activity. Opt. Lett. 28, 2061–2063.

Devor, A., Dunn, A.K., Andermann, M.L., Ulbert, I., Boas, D.A., Dale, A.M., 2003. Coupling of total hemoglobin concentration, oxygenation, and neural activity in rat somatosensory cortex. Neuron 39, 353–359.

Dunn, A.K., Devor, A., Bolay, H., Andermann, M.L., Moskowitz, M.A., Dale, A.M., Boas, D.A., 2003. Simultaneous imaging of total cerebral hemoglobin concentration, oxygenation, and blood flow during functional activation. Opt. Lett. 28, 28–30.

Duong, T.Q., Kim, D.S., Ugurbil, K., Kim, S.G., 2001. Localized cerebral blood flow response at submillimeter columnar resolution. Proc. Natl. Acad. Sci. U. S. A. 98, 10904–10909.

Duong, T.Q., Yacoub, E., Adriany, G., Hu, X.P., Ugurbil, K., Vaughan, J.T., Merkle, H., Kim, S.G., 2002. High-resolution, spin-echo BOLD, and CBF AM at 4 and 7 T. Magn. Reson. Med. 48, 589–593.

Durduran, T., Burnett, M.G., Yu, G.Q., Zhou, C., Furuya, D., Yodh, A.G., Detre, J.A., Greenberg, J.H., 2004a. Spatiotemporal quantification of cerebral blood flow during functional activation in rat somatosensory cortex using laser-speckle flowmetry. J. Cereb. Blood Flow Metab. 24, 518–525.

Durduran, T., Yu, G.Q., Burnett, M.G., Detre, J.A., Greenberg, J.H., Wang, J.J., Zhou, C., Yodh, A.G., 2004b. Diffuse optical measurement of blood flow, blood oxygenation, and metabolism in a human brain during sensorimotor cortex activation. Opt. Lett. 29, 1766–1768.

Erinjeri, J.P., Woolsey, T.A., 2002. Spatial integration of vascular changes with neural activity in mouse cortex. J. Cereb. Blood Flow Metab. 22, 353–360.

Fallgatter, A.J., Strik, W.K., 1998. Frontal brain activation during the Wisconsin Card Sorting Test assessed with two-channel near-infrared spectroscopy. Eur. Arch. Psychiatry Clin. Neurosci. 248, 245–249.

Frahm, J., Merboldt, K.D., Hanicke, W., Kleinschmidt, A., Boecker, H., 1994. Brain or vein—Oxygenation or flow? On signal physiology in functional MRI of human brain activation. NMR Biomed. 7, 45–53.

Franceschini, M.A., Fantini, S., Thompson, J.J., Culver, J.P., Boas, D.A., 2003. Hemodynamic evoked response of the sensorimotor cortex measured non-invasively with near-infrared optical imaging. Psychophysiology 40, 548–560.

Frostig, R.D., Lieke, E.E., Ts'o, D.Y., Grinvald, A., 1990. Cortical functional architecture and local coupling between neuronal activity and the microcirculation revealed by in vivo high-resolution optical imaging of intrinsic signals. Proc. Natl. Acad. Sci. U. S. A. 87, 6082–6086.

Gautama, T., Mandic, D.P., Van Hulle, M.M., 2003. Signal nonlinearity in fMRI: a comparison between BOLD and MION. IEEE Trans. Med. Imaging 22, 636–644.

Grinvald, A., Lieke, E., Frostig, R.D., Gilbert, C.D., Wiesel, T.N., 1986. Functional architecture of cortex revealed by optical imaging of intrinsic signals. Nature 324 (6095), 361–364.

Haskell, R.C., Svaasand, L.O., Tsay, T.T., Feng, T.C., McAdams, M.S., 1994. Boundary-conditions for the diffusion equation in radiative-transfer. J. Opt. Soc. Am. A, Opt. Image Sci. Vis. 11, 2727–2741.

Hebden, J.C., 2003. Advances in optical imaging of the newborn infant brain. Psychophysiology 40, 501–510.

Heekeren, H.R., Obrig, H., Wenzel, R., Eberle, K., Ruben, J., Villringer, K., Kurth, R., Villringer, A., 1997. Cerebral haemoglobin oxygenation during sustained visual stimulation—A near-infrared spectroscopy study. Philos. Trans. R. Soc. Lond., Ser. B Biol. Sci. 352, 743–750.

Hintz, S.R., Cheong, W.F., Van Houten, J.P., Stevenson, D.K., Benaron, D.A., 1999. Bedside imaging of intracranial hemorrhage in the neonate using light: comparison with ultrasound, computed tomography, and magnetic resonance imaging. Pediatr. Res. 45, 54–59.

Hyder, F., Behar, K.L., Martin, M.A., Blamire, A.M., Shulman, R.G., 1994. Dynamic magnetic-resonance-imaging of the rat-brain during forepaw stimulation. J. Cereb. Blood Flow Metab. 14, 649–655.

Iadecola, C., 2004. Neurovascular regulation in the normal brain and in Alzheimer's disease. Nat. Rev., Neurosci. 5, 347–360.

Kak, A.C., Slaney, M., 1988. Principles of Computerized Tomographic Imaging. IEEE Press, New York.

Keller, E., Wietasch, G., Ringleb, P., Scholz, M., Schwarz, S., Stingele, R., Schwab, S., Hanley, D., Hacke, W., 2000. Bedside monitoring of cerebral blood flow in patients with acute hemispheric stroke. Crit. Care Med. 28, 511–516.

Kim, S.G., Ugurbil, K., 2003. High-resolution functional magnetic resonance imaging of the animal brain. Methods 30, 28–41.

Kohl, M., Lindauer, U., Dirnagl, U., Villringer, A., 1998. Separation of changes in light scattering and chromophore concentrations during cortical spreading depression in rats. Opt. Lett. 23, 555–557.

Kohl, M., Lindauer, U., Royl, G., Kuhl, M., Gold, L., Villringer, A., Dirnagl, U., 2000. Physical model for the spectroscopic analysis of cortical intrinsic optical signals. Phys. Med. Biol. 45, 3749–3764.

Kusaka, T., Isobe, K., Nagano, K., Okubo, K., Yasuda, S., Kondo, M., Itoh, S., Onishi, S., 2001a. Estimation of regiona cerebral blood flow distribution in infants by near-infrared topograph using indocyanine green. NeuroImage 13, 944–952.

Kusaka, T., Isobe, K., Nagano, K., Okubo, K., Yasuda, S., Kondo, M., Itoh, S., Onishi, S., 2001b. Functional imaging of the brain in sedated newborn infants using near infrared topography during passive knee movement. Neurosci. Lett. 299, 221–224.

Kusaka, T., Kawada, K., Okubo, K., Nagano, K., Namba, M., Okada, H., Imai, T., Isobe, K., Itoh, S., 2004. Noninvasive optical Imaging in the visual cortex in young infants. Hum. Brain Mapp. 22, 122–132.

Lee, S.P., Duong, T.Q., Yang, G., Iadecola, C., Kim, S.G., 2001. Relative changes of cerebral arterial and venous blood volumes during increased cerebral blood flow: implications for BOLD fMRI. Magn. Reson. Med. 45, 791–800.

Lee, S.P., Silva, A.C., Kim, S.G., 2002. Comparison of diffusion-weighted high-resolution CBF and spin-echo BOLD fMRI at 9.4 T. Magn. Reson. Med. 47, 736–741.

Leite, F.P., Tsao, D., Vanduffel, W., Fize, D., Sasaki, Y., Wald, L.L., Dale, A.M., Kwong, K.K., Orban, G.A., Rosen, B.R., Tootell, R.B.H., Mandeville, J.B., 2002. Repeated fMRI using iron oxide contrast agent in awake, behaving macaques at 3 Tesla. NeuroImage 16, 283–294.

Mandeville, J.B., Marota, J.J., 1999. Vascular filters of functional MRI: spatial localization using BOLD and CBV contrast. Magn. Reson. Med. 42, 591–598.

Mandeville, J.B., Marota, J.J.A., Kosofsky, B.E., Keltner, J.R., Weissleder, R., Rosen, B.R., Weisskoff, R.M., 1998. Dynamic functional imaging of relative cerebral blood volume during rat forepaw stimulation. Magn. Reson. Med. 39, 615–624.

Mandeville, J.B., Marota, J.J., Ayata, C., Zaharchuk, G., Moskowitz, M.A., Rosen, B.R., Weisskoff, R.M., 1999a. Evidence of a cerebrovascular postarteriole windkessel with delayed compliance. J. Cereb. Blood Flow Metab. 19, 679–689.

Mandeville, J.B., Marota, J.J.A., Ayata, C., Zaharchuk, G., Moskowitz, M.A., Rosen, B.R., Weisskoff, R.M., 1999b. Evidence of a cerebrovascular postarteriole windkessel with delayed compliance. J. Cereb. Blood Flow Metab. 19, 679–689.

Mandeville, J.B., Jenkins, B.G., Kosofsky, B.E., Moskowitz, M.A., Rosen, B.R., Marota, J.J.A., 2001. Regional sensitivity and coupling of BOLD and CBV changes during stimulation of rat brain. Magn. Reson. Med. 45, 443–447.

Mayhew, J., Zheng, Y., Hou, Y.Q., Vuksanovic, B., Berwick, J., Askew, S., Coffey, P., 1999. Spectroscopic analysis of changes in remitted illumination: the response to increased neural activity in brain. NeuroImage 10, 304–326.

McGown, A.D., Makker, H., Elwell, C., Al Rawi, P.G., Valipour, A., Spiro, S.G., 2003. Measurement of changes in cytochrome oxidase redox state during obstructive sleep apnea using near-infrared spectroscopy. Sleep 26, 710–716.

Meek, J.H., Firbank, M., Elwell, C.E., Atkinson, J., Braddick, O., Wyatt, J.S., 1998. Regional hemodynamic responses to visual stimulation in awake infants. Pediatr. Res. 43, 840–843.

Miyai, I., Tanabe, H.C., Sase, I., Eda, H., Oda, I., Konishi, I., Tsunazawa, Y., Suzuki, T., Yanagida, T., Kubota, K., 2001. Cortical mapping of gait in humans: a near-infrared spectroscopic topography study. NeuroImage 14, 1186–1192.

Miyai, I., Yagura, H., Hatakenaka, M., Oda, I., Konishi, I., Kubota, K., 2003. Longitudinal optical imaging study for locomotor recovery after stroke. Stroke 34, 2866–2870.

Nemoto, M., Sheth, S., Guiou, M., Pouratian, N., Chen, J.W.Y., Toga, A.W., 2004. Functional signal- and paradigm-dependent linear relationships between synaptic activity and hemodynamic responses in rat somatosensory cortex. J. Neurosci. 24, 3850–3861.

Obata, T., Liu, T.T., Miller, K.L., Luh, W.M., Wong, E.C., Frank, L.R., Buxton, R.B., 2004. Discrepancies between BOLD and flow dynamics in primary and supplementary motor areas: application of the balloon model to the interpretation of BOLD transients. NeuroImage 21, 144–153.

Obrig, H., Hirth, C., Junge-Hulsing, J.G., Doge, C., Wolf, T., Dirnagl, U., Villringer, A., 1996. Cerebral oxygenation changes in response to motor stimulation. J. Appl. Physiol. 81, 1174–1183.

Oleary, M.A., Boas, D.A., Chance, B., Yodh, A.G., 1995. Experimental images of heterogeneous turbid media by frequency-domain diffusing-photon tomography. Opt. Lett. 20, 426–428.

Peng, X.Q., Zhang, C.Y., Alkayed, N.J., Harder, D.R., Koehler, R.C., 2004. Dependency of cortical functional hyperemia to forepaw stimulation on epoxygenase and nitric oxide synthase activities in rats. J. Cereb. Blood Flow Metab. 24, 509–517.

Prahl, S., 2002. Optical Absorption of Hemoglobin. Oregon Medical Laser Center.

Saitou, H., Yanagi, H., Hara, S., Tsuchiya, S., Tomura, S., 2000. Cerebral blood volume and oxygenation among poststroke hemiplegic patients: effects of 13 rehabilitation tasks measured by near-infrared spectroscopy. Arch. Phys. Med. Rehabil. 81, 1348–1356.

Sakatani, K., Chen, S., Lichty, W., Zuo, H., Wang, Y.P., 1999. Cerebral blood oxygenation changes induced by auditory stimulation in newborn infants measured by near infrared spectroscopy. Early Hum. Dev. 55, 229–236.

Sheth, S., Nemoto, M., Guiou, M., Walker, M., Pouratian, N., Toga, A.W., 2003. Evaluation of coupling between optical intrinsic signals and neuronal activity in rat somatosensory cortex. NeuroImage 19, 884–894.

Sheth, S.A., Nemoto, M., Guiou, M., Walker, M., Pouratian, N., Hageman, N., Toga, A.W., 2004a. Columnar specificity of microvascular oxygenation and volume responses: implications for functional brain mapping. J. Neurosci. 24, 634–641.

Sheth, S.A., Nemoto, M., Guiou, M., Walker, M., Pouratian, N., Toga, A.W., 2004b. Linear and nonlinear relationships between neuronal activity, oxygen metabolism, and hemodynamic responses. Neuron 42, 347–355.

Siegel, A.M., Culver, J.P., Mandeville, J.B., Boas, D.A., 2003. Temporal comparison of functional brain imaging with diffuse optical tomography and fMRI during rat forepaw stimulation. Phys. Med. Biol. 48, 1391–1403.

Silva, A.C., Lee, S.P., Yang, G., Iadecola, C., Kim, S.G., 1999. Simultaneous blood oxygenation level-dependent and cerebral blood flow functional magnetic resonance imaging during forepaw stimulation in the rat. J. Cereb. Blood Flow Metab. 19, 871–879.

Sokol, D.K., Markand, O.N., Daly, E.C., Luerssen, T.G., Malkoff, M.D., 2000. Near infrared spectroscopy (NIRS) distinguishes seizure types. Seizure 9, 323–327.

Spielman, A.J., Zhang, G., Yang, C.M., D'Ambrosio, P., Serizawa, S., Nagata, M., von Gizycki, H., Alfano, R.R., 2000. Intracerebral hemodynamics probed by near infrared spectroscopy in the transition between wakefulness and sleep. Brain Res. 866, 313–325.

Stott, J.J., Culver, J.P., Arridge, S.R., Boas, D.A., 2003. Optode positional calibration in diffuse optical tomography. Appl. Opt. 42, 3154–3162.

Taga, G., Asakawa, K., Maki, A., Konishi, Y., Koizumi, H., 2003. Brain imaging in awake infants by near-infrared optical topography. Proc. Natl. Acad. Sci. U. S. A. 100, 10722–10727.

Takahashi, K., Ogata, S., Atsumi, Y., Yamamoto, R., Shiotsuka, S., Maki, A., Yamashita, Y., Yamamoto, T., Koizumi, H., Hirasawa, H., Igawa, M., 2000. Activation of the visual cortex imaged by 24-channel near-infrared spectroscopy. J. Biomed. Opt. 5, 93–96.

Toronov, V., Franceschini, M.A., Filiaci, M., Fantini, S., Wolf, M., Michalos, A., Gratton, E., 2000. Near-infrared study of fluctuations in cerebral hemodynamics during rest and motor stimulation: temporal analysis and spatial mapping. Med. Phys. 27, 801–815.

Tsujimoto, S., Yamamoto, T., Kawaguchi, H., Koizumi, H., Sawaguchi, T., 2004. Prefrontal cortical activation associated with working memory in adults and preschool children: an event-related optical topography study. Cereb. Cortex 14, 703–712.

Vanduffel, W., Fize, D., Mandeville, J.B., Nelissen, K., Van Hecke, P., Rosen, B.R., Tootell, R.B.H., Orban, G.A., 2001. Visual motion processing investigated using contrast agent-enhanced fMRI in awake behaving monkeys. Neuron 32, 565–577.

Vanzetta, I., Slovin, H., Omer, D.B., Grinvald, A., 2004. Columnar resolution of blood volume and oximetry functional maps in the behaving monkey: implications for fMRI. Neuron 42, 843–854.

Villringer, A., Chance, B., 1997. Non-invasive optical spectroscopy and imaging of human brain function. Trends Neurosci. 20, 435–442.

Wray, S., Cope, M., Delpy, D.T., 1988. Characteristics of the near infrared absorption spectra of cytochrome aa3 and hemoglobin for the non-invasive monitoring of cerebral oxygenation. Biochim. Biophys. Acta 933, 184–192.

Yodh, A.G., Boas, D.A., 2003. Functional imaging with diffusing light. In: Vo-Dinh, T. (Ed.), Biomedical Photonics. CRC Press, Boca Raton, pp. 21–45.

Yu, G.Q., Durduran, T., Furuya, D., Greenberg, J.H., Yodh, A.G., 2003. Frequency-domain multiplexing system for in vivo diffuse light measurements of rapid cerebral hemodynamics. Appl. Opt. 42, 2931–2939.

Zaramella, P., Freato, F., Amigoni, A., Salvadori, S., Marangoni, P., Suppjei, A., Schiavo, B., Chiandetti, L., 2001. Brain auditory activation measured by near-infrared spectroscopy (NIRS) in neonates. Pediatr. Res. 49, 213–219.

Zonta, M., Angulo, M.C., Gobbo, S., Rosengarten, B., Hossmann, K.A., Pozzan, T., Carmignoto, G., 2003. Neuron-to-astrocyte signaling is central to the dynamic control of brain microcirculation. Nat. Neurosci. 6, 43–50.